Liu *et al. Cell Communication and Signaling* (2024) 22:378
https://doi.org/10.1186/s12964-024-01759-8

Cell Communication and Signaling

RESEARCH Open Access

Artesunate induces melanoma cell ferroptosis and augments antitumor immunity through targeting Ido1

Wuyi Liu[1†], Huyue Zhou[1†], Wenjing Lai[1], Changpeng Hu[1], Qiaoling Wang[1], Chengsha Yuan[1], Chunmei Luo[1], Mengmeng Yang[1], Min Hu[1], Rong Zhang[1*] and Guobing Li[1*]

Abstract

Artesunate (ART), a natural product isolated from traditional Chinese plant *Artemisia annua*, has not been extensively explored for its anti-melanoma properties. In our study, we found that ART inhibited melanoma cell proliferation and induced melanoma cell ferroptosis. Mechanistic study revealed that ART directly targets Ido1, thereby suppressing Hic1-mediated transcription suppression of Hmox1, resulting in melanoma cell ferroptosis. In $CD8^+$ T cells, ART does not cause cell ferroptosis due to the low expression of Hmox1. It also targets Ido1, elevating tryptophan levels, which inhibits NFATc1-mediated PD1 transcription, consequently activating $CD8^+$ T cells. Our study uncovered a potent and synergistic anti-melanoma efficacy arising from ART-induced melanoma cell ferroptosis and concurrently enhancing $CD8^+$ T cell-mediated immune response both in vivo and in vitro through directly targeting Ido1. Our study provides a novel mechanistic basis for the utilization of ART as an Ido1 inhibitor and application in clinical melanoma treatment.

Keywords Artesunate, Melanoma, Ferroptosis, $CD8^+$ T cell, Ido1

Introduction

Melanoma, an aggressive malignancy originating from pigment-producing melanocytes, is primarily localized at the epidermal-dermal junction in human skin, contributing significantly to skin cancer-related fatalities [1]. Although surgery can often cure primary melanomas in the early stages, approximately 20% of patients still advance to metastatic disease [2]. Despite substantial achievements in current therapeutic strategies such as targeted therapy and immunotherapies, many patients fail to benefit due to low response rates, extensive adverse events and drug resistance. Thus, the development of novel therapeutic drugs and clarification of their anti-melanoma mechanism are imperative to improve the clinical outcomes of melanoma patients.

Ferroptosis is a newly discovered form of non-apoptotic cell death characterized by iron-dependent lipid peroxidation [3]. The accumulation of reactive oxygen species (ROS) and free iron leads to lipid peroxidation, which ultimately triggers ferroptosis [4]. In the pursuit of proliferation and progression, cancer cells harbor higher levels of catalytic Fe^{2+} than normal cells, suggesting the induction of ferroptosis may selectively inhibit tumor proliferation and progression [4]. Recent studies have increasingly demonstrated that ferroptosis exerts inhibitory effects on cancer cell growth across various

†Wuyi Liu and Huyue Zhou contributed equally to this work.

*Correspondence:
Rong Zhang
zrcq73@tmmu.edu.cn
Guobing Li
guobingl@tmmu.edu.cn
[1]Department of Pharmacy, The Second Affiliated Hospital of Army Medical University, Chongqing 400037, China

malignancies [5, 6]. Therefore, targeting ferroptosis to eliminate tumors is considered a promising strategy for cancer therapy.

Traditional Chinese medicine (TCM) have a long history of clinical practice, and in recent years, they have garnered increased attention for their promising anticancer potential. In clinical, many anticancer drugs are obtained from natural products or their derivatives [7]. Artesunate (ART), a water-soluble semi-synthetic derivative of artemisinin, was first discovered by Youyou Tu in 1972 from *Artemisia annuaL*. Beyond its traditional anti-malarial effect, recent studies have unveiled numerous bioactivities of ART, including anti-inflammatory, anti-viral, especially anticancer effects both in vitro and in vivo [8–11]. Moreover, ART has demonstrated robust antitumor effects in select types of cancers with minimal toxicity towards normal cells, which has also been proved in clinical trials [12–14]. However, studies investigating the effects of ART on melanoma are scarce, and the underlying molecular mechanisms of its anticancer effects remain unclear.

Recently, ART was found to regulate immune cells and promote antitumor immunity [15, 16]. Considering the importance of immune-evasion in melanoma therapy and the central contribution of $CD8^+$ T cells to the anti-tumor immune response, it is essential to explore whether ART affects $CD8^+$ T cell function and remodels the tumor microenvironment (TME). Indoleamine2,3-dioxygenase 1 (Ido1), a cytosolic heme-containing enzyme, catabolizes the degradation of tryptophan (Trp) and the production of Kynurenine (Kyn). Ido1 is frequently overexpressed in various cancer types, exhibiting an inverse correlation with the overall survival of cancer patients [17–20]. Ido1 promotes the immunosuppressive regulatory T cells (Tregs) and suppresses $CD8^+$ T effector cells, facilitating an immunosuppressive microenvironment [21–23]. Thus, Ido1 emerges as an attractive target for anticancer drug development [24]. Recent findings indicate that Ido1 inhibitors possess anticancer effects in preclinical models, clinical trials, thus, the clinical application of Ido1 inhibitors would enhance the outcomes of cancer treatment [25, 26].

In this study, we found that ART effectively inhibits the proliferation of multiple melanoma cells and induces ferroptosis by elevating ROS and MDA production, along with lipid peroxidation. Mechanistically, ART triggers ferroptosis in melanoma cells by directly targeting Ido1, consequently suppressing Hic1-mediated transcription suppression of Hmox1. Moreover, ART also actives $CD8^+$ T cells by targeting Ido1, thereby increasing tryptophan, decreasing NFATc1, inhibiting the transcription of PD1 and finally enhancing effector function of $CD8^+$ T cells. Our study provided a novel mechanistic basis for the application of ART in the treatment of melanoma.

Materials and methods

Reagents and antibodies

Artesunate (HY-N0193) was purchased from MedChemExpress (MCE), Ferrostatin-1 (Fer-1, S7243) and Erastin (S7242) were purchased from Selleck. BODIPY 581/591 C11 (D3861) was purchased from Thermo Fisher Scientific. FerroOrange (F374) was purchased from DOJINDO.

Cell culture

Cell lines (B16F10, SK-MEL-28) in this study were obtained from American Type Culture Collection (ATCC, USA). Cells were grown in DMEM supplemented with 10% fetal bovine serum (Lonsera, S711-001) added and Penicillin-Streptomycin Solution (Beyotime, C0222). Then cells were cultured in an incubator at 37℃ and 5% CO_2.

Cell viability assay and morphological observation

Cells were seeded into a 96-well plate and cultured overnight. Cell medium was replaced and cultured with different concentrations of ART (0, 10, 20, 40, 80,160 μM) for 24 h. After arriving the time point, the Cell Counting Kit-8 (CCK-8, Beyotime, C0039) reagent (10 μL) was added into each well and cultured for another 1 h. Absorbance at 450 nm was measured using a microplate reader. The cell viability was presented as mean ± SD at the percentage of control. For examination of morphological changes, cells were treated with ART and the changes of cell morphology were observed under the inverted microscope (Olympus, Tokyo, Japan).

Clone formation assay

Crystal violet was employed to detect colony formation. B16F10 and SK-MEL-28 cells were inoculated into a 5-cm dish at a concentration of 200 cells/well. The next day, cells were treated with ART at 0, 10, 20, 40 μM for 24 h. After cultured for 14 days (during which the medium was changed each 3 days), cells were washed with PBS and fixed for 15 min. After that, clones were stained with 0.2% crystal violet and colonies were photographed. Three independent experiments were performed.

Immunofluorescence

After treated with different concentrations of ART, cells were washed and fixed, then permeabilized with 0.5% Triton X-100. Later, cells were stained with primary antibodies at 4℃ overnight. On the next day, they were cultured with related secondary antibodies coupled with Alexa 488 for 1 h at 37℃. DAPI were used to stain the nuclei and the immunofluorescence were examined by fluorescence microscopy (Olympus, Japan).

Cell cycle analysis

After treated with different concentrations of ART (0, 10, 20, 40 μM), cells were harvested and fixed with 75% cold ethanol and stored at -20℃ overnight. Then, the cells were incubated with propidium iodide in the dark for 30 min and the cell cycle was analyzed by flow cytometry on a BD Fortessa cytometer.

Western blot analysis

Cell proteins were extracted with cell lysis buffer (Beyotime, P0013) containing with the protease inhibitor PMSF (Beyotime, ST506) and separated with 10% sulfate-polyacrylamide gel electrophoresis (SDS-PAGE). The proteins were then transferred onto a PVDF membrane for 3 h at 400 mV. After that, the membrane was blocked in 5% non-fat milk prepared with TBST buffer at room temperature for 2 h. Then, membranes were incubated with related primary antibodies (Supplementary Table 1) at 4℃ overnight. On the next day, the membrane was washed with TBST for three times and incubated with the horseradish peroxidase (HRP)-conjugated secondary antibodies at room temperature for 2 h. Then, the membranes were washed three times with TBST and finally visualized by Clarity Western ECL Sbustrate (Bio-Rad, 1,705,061).

RNA-sequencing analysis

B16F10 or $CD8^+$ T cells were seeded on 6-well plates and treated with 20 μM ART. Subsequently, the total RNA was extracted using Trizol reagent (Takara, 9109) for whole-genome transcriptome profiling by RNA-sequencing. Each group included three replicates. The quality control, library construction and RNA-sequencing experiments were performed by BGI (Beijing Genomics Institute). The differentially expressed genes (DEGs) were screened using R software with a cut-off of $|\log_2(\text{fold change})| > 1$ and $P\text{-value} < 0.05$. Gene set enrichment analysis (GSEA) was performed by the Broad Institute GSEA version 3.0 software using gene sets downloaded from the Molecular Signatures Database (MsigDB). Normalized enrichment score (NES) and false discovery rate (FDR) were used to determine the statistical significances according to a previous report [27]. The functional analysis of the DEGs were performed by the Gene Ontology (GO) enrichment analyses.

Reactive oxygen species (ROS) assay

The production of ROS was assessed by ROS-specific fluorescent probe 2',7'-Dichlorofluorescin diacetate (DCFH-DA) kit (Beyotime, S0033M). Briefly, cells were treated with ART at 0, 10, 20, 40 μM for 24 h, then washed with PBS, and incubated with 10 μM DCFH-DA for 30 min at 37℃ in the dark. The ROS levels were detected with a flow cytometer or observed under a fluorescence microscope.

Detection of intracellular ferrous iron content

To detect intracellular ferrous ions, cells were grown on 24-well cell culture plates, washed with PBS and cultured with 1 μM FerroOrange (Dojindo, F374) for 30 min at 37℃. Finally, the fluorescence was observed by fluorescence microscope.

Determination of lipid peroxidation

Cells were cultured in 6-well plate and treated with different concentrations of ART (0, 10, 20, 40 μM). Cells were harvested for BODIPY 581/591 C11 (Thermo Fisher, D3861) staining for 30 min in 37℃ to detect lipid peroxidation. Cells were washed twice with PBS, then the fluorescence intensity was detected using flow cytometry. Results were analyzed by FlowjO V10 software, and the mean fluorescence intensity (MFI) of oxidized C11 (FITC) was calculated. All data were normalized to the control samples.

Measurement of malondialdehyde (MDA)

Cellular MDA contents were assessed by cell malondialdehyde (MDA) assay kit (Beyotime, S0131M). In brief, cells were cultured in a 6-well plate overnight, and then treated with ART (0, 10, 20, 40 μM) for 24 h. Cells were harvested, lysed and protein were quantified. After that, MDA working solution was added and heated, the supernatant was collected. Finally, the level of MDA was measured at 532 nm using a microplate reader.

Real-time PCR

Total RNA was extracted from cells using Trizol reagent. Real-time PCR amplification was performed using an ABI PRISM 7900 thermocycler with SYBR Premix Taq (Applied Biosystems) according to the manufacturer's protocol. The threshold cycle (CT) values for each gene were normalized to those of Actin, and the $2^{-\Delta\Delta CT}$ method were employed for quantitative analysis. The primers used in this study were shown in Supplementary Table 2.

CRISPR/Cas9 mediated gene knockout

The gene sequence of Hmox1/Hic1/Creb1/Ido1 was obtained from the NCBI database, and the appropriate Hmox1/Hic1/Creb1/Ido1 sgRNAs were synthesized from Shanghai Sangon Co., Ltd (Shanghai, China). Their sequences are shown in Supplementary Table 2. sgRNAs were assembled into Lenti-V2 CRISPR/Cas9 backbone (Addgene, 52961) and then transfected into cells using Lipo8000 (Beyotime, C0533) according to the manufacturer's instructions. After that, monoclonal cells with CRISPR/Cas9-mediated Hmox1, Hic1, Creb1 or Ido1

deletion were screened and the gene editing was verified by sanger sequencing.

Dual-luciferase reporter assay

The promoter region of Hmox1 was amplified and product was inserted into the luciferase vector pGL6-TA (Beyotime, D2105) to construct the Hmox1 promoter reporter plasmid pGL6-TA-Hmox1. Finally, pGL6-TA-Hmox1 firefly luciferase reporter plasmid and Renilla luciferase reporter plasmid were co-transferred into B16F10 cells using Lipo8000. After 24 h post-transfection, cell lysates were assayed for luciferase activity using Dual-Luciferase Assay system according to the manufacturer's instructions (Beyotime, RG017 and RG010M) and the luciferase activity of the reporter gene was normalized to Renilla luciferase activity.

Chromatin immunoprecipitation (CHIP) assay

A commercial CHIP kit (Beyotime, P2083S) was used for CHIP assay. Briefly, B16F10 cells were fixed with PFA for 10 min' crosslink, followed by sonication to fragment the DNA into lengths ranging from 100 to 800 bp. Next, DNA fragments were mixed with IgG or Hic1 antibody for immunoprecipitation over night at 4℃. Then, the precipitated chromatin fragments were collected, purified and analyzed through PCR. PCR products were electrophoresed on 2% agarose gels.

Molecular docking

The structure of ART in sdf format was downloaded from the PubChem database and transformed into a three-dimensional structure by ChemBio3D energy minimization saved as mol2 format. Then, the 3D structure of Ido was downloaded from PDB database and PyMol software was used to delete the water molecule as well as the original ligand. Afterwards, Ido protein was used as receptor and ART molecule as ligand, the active sites of molecular docking were determined by the coordinates of the ligands in the target protein complex, followed by molecular docking using AutoDock Vina, and mapping correlation by PyMol.

Surface plasmon resonance (SPR) assay

Biacore T200 (Cytiva, United States) and Sensor Chip CM5 (Cytiva, United States) were used for the measurement of the interaction of ART with Ido1. Mouse Ido1 protein (Sino Biological, 57,213-M08E) was diluted to final concentration of 20 μg/mL with pH 4.0 sodium acetate. On the experimental channel Fc2, the mixture of EDC (0.2 mol/L) and NHS (50 mmol/L) at a ratio of 1:1 was used to activate the surface of the CM5 chip for 420 s. After the horizontal ~ 12400RU was fixed, it flowed through Ethanolamine on the chip surface to seal the excess sites. The reference channel Fc1 was directly blocked after activation. Moreover, ART was diluted to 50, 25, 12.5, 6.25, 3.125 μM with Running buffer. The analyte flows through both the experimental channel and the reference channel. The obtained data were fitted according to the analysis software, the time as the abscissa and the response value as the ordinate to analyze the binding kinetics between ART and Ido1.

Cellular thermal shift assay (CETSA)

After treated with ART for 24 h, B16F10 cells were lysed and centrifuged. Then the supernatant was divided into five aliquots and individually heated at various temperatures (40, 44, 48, 52 and 56℃) for 3 min, followed by rapid cooling at 4℃. Subsequently, the cell lysates were detected by western blotting with Ido1 antibody.

Mouse tumor models

Animal experiments were followed the guidance of the Institutional Animal Care and Use Committee of Army Medical University. 1×10^5 B16F10 cells in serum-free medium were subcutaneously injected into the right flanks of six-week-old female C57 mice. When the tumor volume reached 100 mm^3, mice were randomly divided into three groups: control group ($n=5$), ART (100 mg/kg/day, $n=5$), ART (200 mg/kg/day, $n=5$). Tumor size and body weight were measured each 2 days. Tumor volumes were calculated by length×$width^2$/2. Mice were sacrificed and tumors were collected and weighted after 9 days following injection. Tumors were fixed with 10% formalin and embedded in paraffin for immunohistochemical staining. For $CD8^+$ T cell depletion, mice were *i.p.* injected with *InVivo*Mab anti-mouse CD8α (BioXCell, BE0117) antibody or corresponding isotype control (200 μg per dose per mouse) on day −13 and −6.

Flow cytometry of tumor tissues

Tumor tissues were homogenized and digested. Single cell suspension was filtered and then subjected to discontinuous Percoll (Cytiva, 17089109) gradient centrifugation to isolate lymphocyte-enriched compartments. From the middle cloudy layer, we got the immune cells. Red blood cells were lysed by Red Blood Cell Lysis Buffer (Beyotime, C3702). Cells were added with CD107a, then incubated with Brefeldin A (Invitrogen, 00-4506-51) and Monensin (Invitrogen, 00-4505-51) for another 6 h. Then, cells were labeled with biomarkers: CD45, CD3, CD4, CD8, PD1, CD69, TNFα, IFNγ (listed in Supplementary Table 1) for subsequent flow cytometry detection. Samples were detected on a flow cytometer (BD LSRFortessa™) and the results were analyzed by the FlowJo V10.3 software.

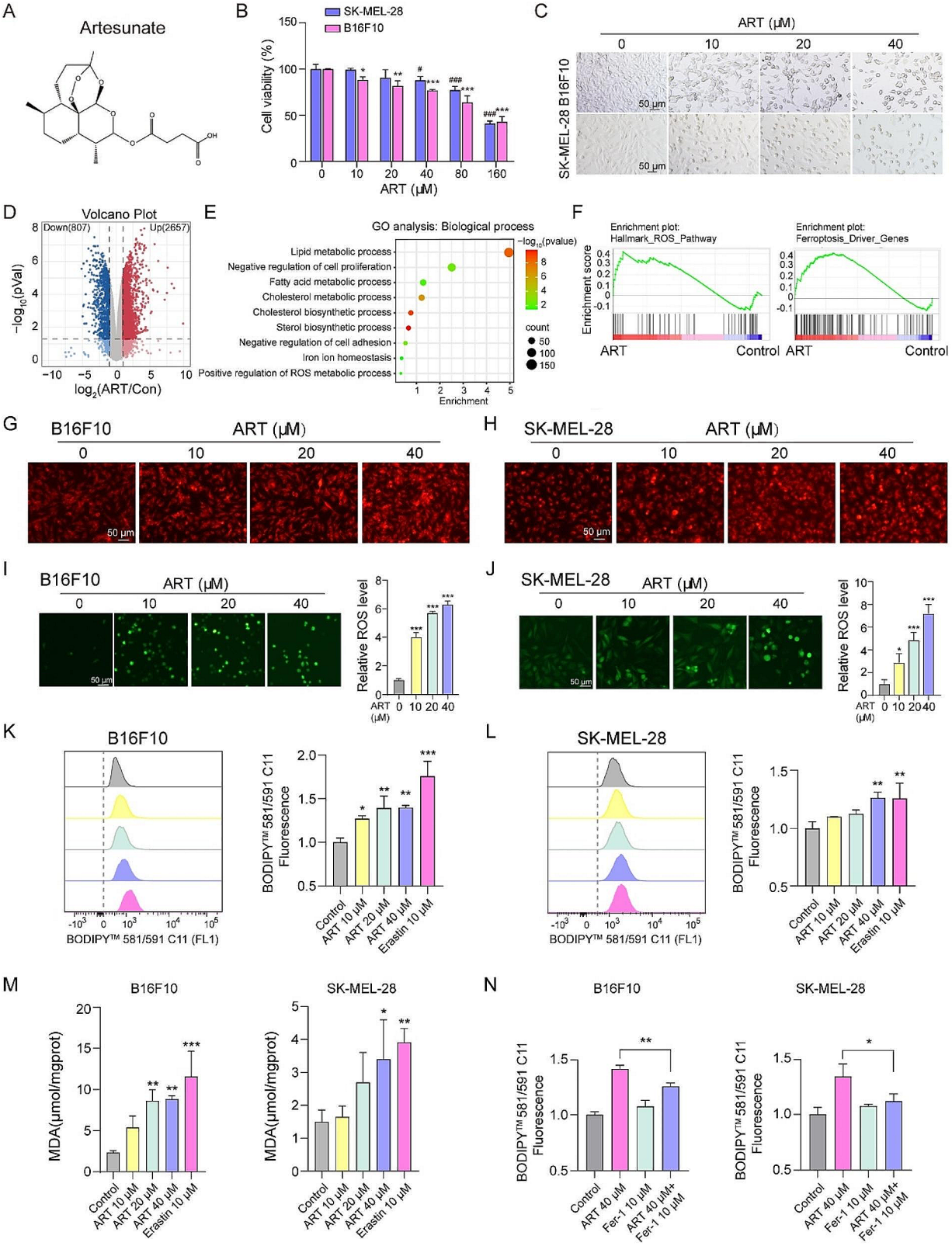

Fig. 1 (See legend on next page.)

(See figure on previous page.)

Fig. 1 ART induced melanoma cells ferroptosis. (**A**) The chemical structure of ART was displayed. (**B**) B16F10 and SK-MEL-28 cells were treated with different concentrations of ART (0, 10, 20, 40, 80,160 μM) for 24 h, cell viability was assessed by CCK8 assay. (**C**) B16F10 and SK-MEL-28 cells were treated with different concentrations of ART (0, 10, 20, 40 μM) for 24 h, cell morphological alterations were observed. (**D**) The volcano plot of RNA-seq. (**E**) GO analysis: Biological process of differentially expressed genes (DEGs). (**F**) GSEA analysis of RNA-seq data. (**G** and **H**) B16F10 cells and SK-MEL-28 cells were treated with indicated concentrations of ART (0, 10, 20, 40 μM) for 24 h, cells were stained with FerroOrange and photographed by fluorescence microscopy. (**I** and **J**) Fluorescence microscopy and flow cytometry were used to detect the ROS levels by staining with DCFH-DA probe. (**K** and **L**) Cells were treated with indicated concentrations of ART (0, 10, 20, 40 μM) or Erastin (10 μM) for 24 h, flow cytometry detected the lipid peroxidation level by staining with C11-BODIPY. (**M**) Levels of malondialdehyde (MDA) in cells. (**N**) Cells were treated with ART (40 μM) and/or Fer-1 (10 μM) for 24 h, flow cytometry detected the lipid peroxidation. $^{*}P<0.05$; $^{**}P<0.01$; $^{***}P<0.001$; $^{\#}P<0.05$; $^{\#\#\#}P<0.001$

Isolation and activation of splenic CD8$^+$ T cells

CD8$^+$ T cells were isolated from mouse spleens using the EasySep™ Mouse CD8$^+$ T Cell Isolation Kit (Stemcell, 19853). These cells were subsequently seeded into 6-well plates pre-coated with anti-CD3 monoclonal antibody (2.5 μg/mL, eBioscience, 16-0032-86) in the presence of soluble anti-CD28 monoclonal antibody (1 μg/mL, eBioscience, 16-0281-86) and 200 U/mL mouse interleukin-2 (IL-2, PEPROTech, 212−12). Then, CD8$^+$ T cells were cultured for another 3 days to achieve activation before further use.

CD8$^+$ T cell-mediated tumor cell killing assay

B16F10 cells were co-cultured with activated CD8$^+$ T cells to assess the cytotoxicity of CD8$^+$ T cells, then determined using the CCK8 assay. In brief, B16F10 cells and CD8$^+$ T cells were separately treated with ART for 24 h, followed by co-culturing B16F10 cells with activated CD8$^+$ T cells for 48 h, Then, the CD8$^+$ T cells were collected and washed, CCK8 solution (10 μL) was added to each well, incubating for an additional 2 h. Cell viability was analyzed at 450 nm through a microplate reader [28]. Furthermore, the CD8$^+$ T cells were harvested for flow cytometry.

Enzyme-linked immunosorbent assay

CD8$^+$ T cells were plated in a 6-well plate overnight. On the next day, cells were pretreated with ART (20 μM) or Epa (100 nM) for 24 h. Finally, the supernatant was collected for the determination of Tryptophan (Meimian, MM-0756M1), Kynurenine (FineTest, EM1862), TNFα (Boster, EK0527) and IFNγ (Boster, EK0375) by the ELISA kit following the manufacturer's instructions.

Bioinformatic analysis

Ferroptosis driver genes were downloaded from the FerrDb database (http://www.zhounan.org/ferrdb/current/). The list of ferroptosis-driver genes was shown in Supplementary Table 3. A protein-protein interaction (PPI) network was constructed based on the string database (https://cn.string-db.org/). Cytoscape software was used to visualize the PPI network and screen the hub genes with the Cytoscape plugin cytoHubba [29]. Potential transcription factors of Hmox1 were predicted by multiple tools, including JASPAR (https://jaspar.elixir.no/), Animal TFDB (http://bioinfo.life.hust.edu.cn/AnimalTFDB/#!/) and GeneHancer (https://www.genecards.org/). The SDF file of ART (Compound CID: 6917864) was downloaded from the Pubchem database (https://pubchem.ncbi.nlm.nih.gov/). SwissTarget (http://www.swisstargetprediction.ch/) and SuperPRED prediction web server [30] (https://prediction.charite.de/subpages/target_prediction.php) and chEMBL (https://www.ebi.ac.uk/chembl/) were used to predicate the potential target of ART. The symbol corresponding to the protein target name was standardized using the uniProt database (https://www.uniprot.org/).

Statistical analysis

Statistical analysis was performed using GraphPad Prism 8.0 software. All data were expressed as the mean ± SD. The t-test was used for comparison of two groups. One-way or two-way analysis of variance (ANOVA) was used for multiple groups comparison. All experiments were conducted at least in triplicate. The results were considered significant at $^{*}p<0.05$, $^{**}p<0.01$, $^{***}p<0.001$.

Results

ART induced melanoma cells ferroptosis

To assess the cytotoxic effects of ART (Fig. 1A) on melanoma cells, melanoma B16F10 and SK-MEL-28 cells were treated with different concentrations of ART (0, 10, 20, 40, 80, 160 μM) for 24 h, and results of CCK8 assay revealed that ART inhibited the cell viability of both B16F10 and SK-MEL-28 cells in a dose-dependent manner (Fig. 1B). Microscopic observation displayed that ART dependently caused notable morphological alterations, like reduced cell number, cell volume and cell-cell junction (Fig. 1C). In order to explore the underlying mechanisms of ART-induced cancer cell inhibition. B16F10 cell were treated with or without ART, RNA-sequencing analysis (RNA-seq) was performed and the volcano plot was shown (Fig. 1D). The results of enrichment analysis of Gene Ontology (GO) revealed that the differentially expressed genes (DEGs) were mainly enriched in Lipid metabolic process, Negative regulation of cell proliferation, Fatty acid metabolic process, etc. (Fig. 1E). First, we confirmed that ART significantly inhibited melanoma cell proliferation by analyzing the cell proliferation-related makers in the RNA-seq data,

clone formation assay and Ki67 staining (Supplementary Figs. 1–2). Additionally, our data showed that ART induced melanoma cell cycle arrest at the G2/M phase (Supplementary Fig. 3). Next, our RNA-seq data demonstrated that ART did not affect the expression of apoptosis-related makers (Supplementary Fig. 4), while ART significantly increased the expression of ferroptosis driver markers (Supplementary Fig. 5). Furthermore, Gene Set Enrichment Analysis (GSEA) analysis also indicated that ART treatment obviously enriched in the ROS_Pathway and Ferroptosis_Driver_Genes (Fig. 1F). To validate the RNA-seq findings, we employed FerroOrange, a Fe^{2+} iron probe, to access the intracellular Fe^{2+} levels, and we observed an obviously increase in orange fluorescence in ART-treated cells (Fig. 1G-H). Since the cytotoxicity of ferroptosis is dependent on ROS production, cytotoxicity [31], we evaluated ROS levels following ART treatment using the DCFH-DA probe. Flow cytometry results showed that ART dose-dependently increased the generation of ROS in SK-MEL-28 and B16F10 cells (Fig. 1I-J). Meanwhile, melanoma cells were labeled with the lipid peroxidation sensor C11-BODIPY, and we confirmed that ART dose-dependently increased the lipid peroxidation (Fig. 1K-L). We also measured lipid peroxidation by detecting the levels of malondialdehyde (MDA), which is an end-product of lipid peroxides. The results were in consistent with our previous finding that ART significantly promoted the generation of MDA in a dose-dependent manner (Fig. 1M). Moreover, we found that ART-induced ferroptosis can be reversed by ferroptosis inhibitor ferrostatin-1 (Fer-1) (Fig. 1N). Collectively, our findings demonstrate that ART effectively inhibits melanoma cell proliferation and induces ferroptosis by elevating ROS and MDA production, along with lipid peroxidation.

ART induced melanoma cell ferroptosis is dependent on Hmox1

To explore the underlying mechanisms of ART-induced melanoma cell ferroptosis, we used a Venn diagram to overlap upregulated DEGs with ferroptosis driver genes downloaded from the FerrDb database, resulting in the intersection of 19 genes (Fig. 2A). Their expression was displayed in Fig. 2B. The protein-protein interaction (PPI) network was generated by String website and Cytoscape, and based on the scores and degrees in cytoHubba method, we proposed that Hmox1 may be the key target for ART-induced melanoma cell ferroptosis (Fig. 2C-D). To further verify the role of Hmox1, qPCR assay was performed and we found that the Hmox1 was dose-dependently upregulated in ART-treated B16F10 cells (Fig. 2E), and this increasing expression was confirmed by immunofluorescence and western blot (Fig. 2F-G). Subsequently, to confirm the role of Hmox1 in ART-induced ferroptosis, we utilized the Crispr-Cas9/gRNA method to knock out Hmox1 in B16F10 cells, confirming knockout efficiency via western blot (Fig. 2H). Hmox1 knockout significantly suppressed the ferroptosis indicators including ROS, MDA production and lipid peroxidation, while slightly increased cell proliferation in B16F10 cells (Supplementary Fig. 6). Additionally, Hmox1 knockout further abrogated ART-induced increases in ROS, lipid peroxidation and MDA production (Fig. 2I-K). Furthermore, we constructed a Hmox1-overexpression plasmid and found that Hmox1 overexpression in B16F10 cells significantly enhanced ART-induced ferroptosis, as evidenced by the increased ROS, lipid peroxidation and MDA production (Fig. 2L-O). Taken together, these results suggest that ART-induced ferroptosis in melanoma cells is dependent on Hmox1.

ART directly targets Ido1, inhibiting Hic1-mediated transcription suppression of Hmox1

The regulatory mechanism by which ART increases Hmox1 transcription is unclear. We first predicted the transcription factors of Hmox1 using three online transcription factor prediction tools: JASPAR, Animal TFDB and GeneHancer, followed by overlapping with DEGs, revealing two candidate genes that may regulate the transcription of Hmox1: Creb1 and Hic1 (Fig. 3A). The JASPAR predicted scores of Creb1 and Hic1 were shown in Fig. 3B. Our western blot reminded us that ART dose-dependently downregulated the expression of Hic1 (Fig. 3C). Conversely, no significant correlation was observed between Creb1 and Hmox1, and our qPCR indicated that Creb1 knockout had no effect on Hmox1 mRNA expression (Supplementary Fig. 7). Subsequently, we knocked out Hic1 in B16F10 cells and observed a significantly increase in the mRNA levels of Hmox1 (Fig. 3D-E), indicating that Hic1 may act as a transcriptional suppressor of Hmox1. To validate the transcriptional repression role of Hic1 on Hmox1, luciferase reporter gene assays were performed. The Hmox1 promoter was cloned into a luciferase expression vector and co-transferred with Renilla luciferase reporter plasmid into B16F10 cells. Results showed that Hic1 knockout substantially enhanced the Hmox1 promoter activity (Fig. 3F). Then, six Hmox1 promoter fragments (P1 to P6) were cloned into luciferase vectors (Fig. 3G). Among them, P6 emerged as the pivotal fragment regulating Hmox1 transcription under the influence of Hic1. P1, P3 and P5 fragments without P6 sequence effectively blocked the increased luciferase activity resulting from Hic1 knockout (Fig. 3H). Furthermore, three Hic1 binding sites in P6 were predicted by JASPAR, and their deletion mutant luciferase plasmids were constructed. We further clarified that the deletion of site 2 completely abolished the increased luciferase activity associated

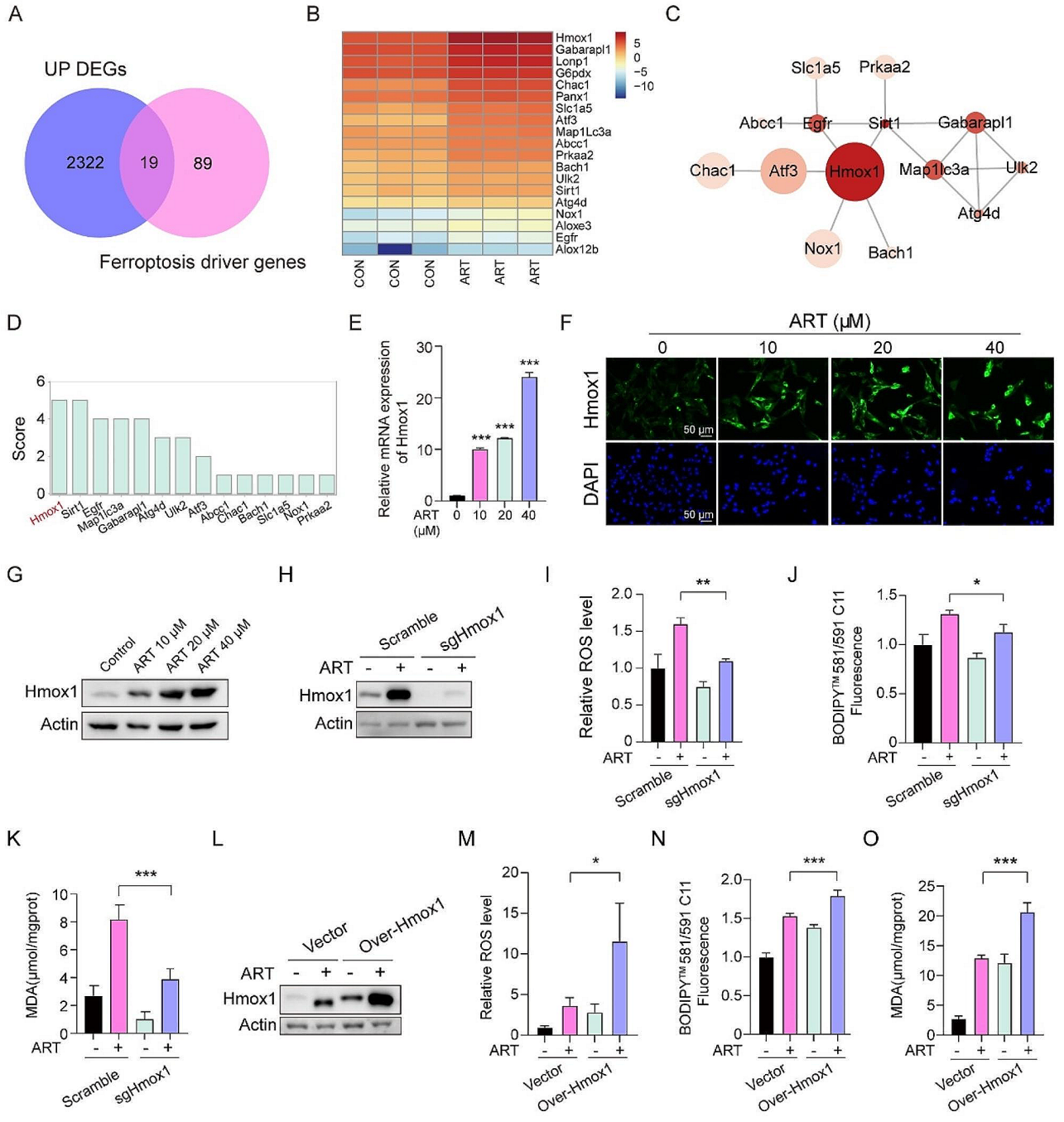

Fig. 2 ART induced melanoma cell ferroptosis is dependent on Hmox1. (**A**) The Venn diagram of UP DEGs and Ferroptosis driver genes. (**B**) Heatmap for the 19 overlapping genes. (**C**) The PPI network of these overlapping genes. (**D**) Cytohubba scores were displayed. (**E**) qPCR detected the mRNA expression of Hmox1 in ART-treated B16F10 cells. (**F** and **G**) Fluorescence microscopy and western blot was employed to detect the expression of Hmox1 in ART-treated B16F10 cells. (**H**) western blot assay detected the expression of Hmox1 in B16F10 cells after Crispr-cas9/gRNA knockout. The ROS levels (**I**), The lipid peroxidation (**J**) and the MDA levels (**K**) in B16F10 Scramble and sgHmox1 cells after ART treatment (20 μM). (**L**) Hmox1-overexpression plasmid was constructed and transferred into B16F10 cells, western blot assay detected the expression of Hmox1 after ART treatment (20 μM). The ROS levels (**M**), The lipid peroxidation (**N**) and the MDA levels (**O**) in B16F10 Vector and Over-Hmox1 cells. *$P < 0.05$; **$P < 0.01$; ***$P < 0.001$

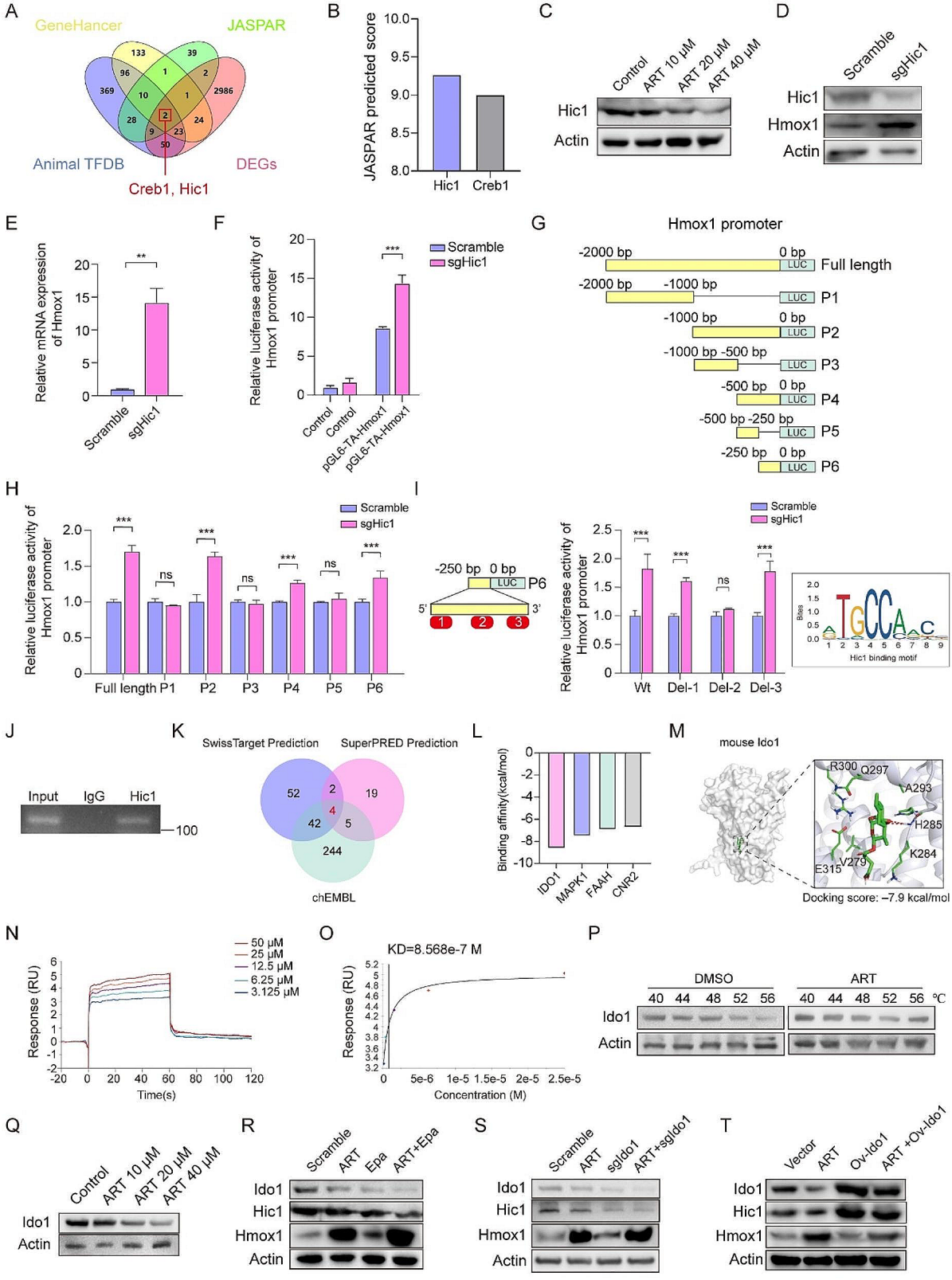

Fig. 3 (See legend on next page.)

(See figure on previous page.)

Fig. 3 ART directly targets Ido1, inhibiting Hic1-mediated transcription suppression of Hmox1. (**A**) The results of three online transcription factor prediction tools: JASPAR, Animal TFDB and GeneHancer were intersected with DEGs. (**B**) JASPAR predicted scores of Hic1 and Creb1. (**C**) Hic1 expression in ART-treated B16F10 cells. (**D**) Knockout of Hic1 in B16F10 cells and the expression of Hic1 and Hmox1 was detected by western blot. (**E**) qPCR detected the mRNA expression of Hmox1 in Hic1 knockout B16F10 cells. (**F**) Luciferase reporter assay of Homx1 promoter with Hic1 knockout. (**G**) Schematic of Hmox1 promoter fragments luciferase plasmids construction. (**H**) Luciferase activity of different Hmox1 promoter fragments (Full length, P1, P2, P3, P4, P5, P6) were detected after Hic1 knockout. (**I**) Luciferase reporter assay of site deletion plasmids of P6, and the sequence of Hic1 binding site. (**J**) The CHIP assay confirmed the direct binding site of Hic1 on Hmox1 promoter. (**K**) The ART potential target predication from SwissTarget prediction, SuperPRED and chEMBL websites. (**L**) Molecular docking results of ART with 4 human potential targets. (**M**) Molecular docking of ART with mouse Ido1. (**N** and **O**) SPR assay detected the kinetics/affinity between ART with Ido1. (**P**) CETSA assay for detecting the stability of the Ido1 protein in the presence of ART. (**Q**) Ido1 expression in B16F10 cells treated with different concentrations of ART. (**R**) After B16F10 cells were treated with ART and/or Ido1 inhibitor Epacadostat (Epa), the expression of Ido1, Hic1 and Hmox1 was detected by western blot. (**S**) The expression of Ido1, Hic1 and Hmox1 after Ido1 knockout and/or ART treatment. (**T**) The expression of Ido1, Hic1 and Hmox1 in Ido1-overexpressed B16F10 cells treated with or without ART. $^{**}P < 0.01$; $^{***}P < 0.001$

with Hic1 knockout (Fig. 3I). Additionally, amplification primers were designed at the left and right of site 2, and CHIP experiments using anti-Hic1 were performed, conclusively confirming site 2 as the binding site for Hic1 (Fig. 3J).

Identifying the direct targets of a drug is particularly important for elucidating its mechanism. We intersected 4 potential targets of ART from SwissTarget prediction, SuperPRED and chEMBL (Fig. 3K). And these 4 potential targets were individually molecular docking with ART, with Ido1 having the highest absolute affinity score with ART (Fig. 3L). ART exhibits a strong affinity not just for mouse Ido1 (Fig. 3M), but also for human IDO1 (Supplementary Fig. 8).

The kinetics/affinity between ART and Ido1 were further determined by the SPR assay. SPR results indicated that ART exhibited concentration-dependent binding responses with Ido1 protein in vitro (Fig. 3N). And the results illustrated a KD value of 8.568e-7 M, underscoring the robust interaction capability between ART and Ido1 (Fig. 3O). Furthermore, the CETSA assay indicated increased stability of the Ido1 protein in the presence of ART across a range of temperatures (40, 44, 48, 52, 56℃) (Fig. 3P). Western blot assay results demonstrated a dose-dependent downregulation of Ido1 induced by ART (Fig. 3Q). To validate the pivotal role of Ido1 in ART-mediated Hic1 suppression and Hmox1 upregulation, we proceeded to knockout Ido1 in B16F10 cells or treated cells with the Ido1 inhibitor Epacadostat (Epa). The results revealed that the ART-induced downregulation of Ido1/Hic1 was further attenuated, and the ART-induced upregulation of Hmox1 was further enhanced (Fig. 3R-S). Conversely, overexpression of Ido1 in B16F10 cells effectively reversed the ART-induced downregulation of Ido1/Hic1 and the upregulation of Hmox1 (Fig. 3T). These findings collectively indicate that ART directly targets Ido1, resulting in the suppression of Hic1 and consequent elevation in the transcription of Hmox1.

ART enhanced effector function of $CD8^+$ T cells in vitro through targeting Ido1

Recently, ART was reported to regulate immune cells and promote antitumor immunity [15, 16]. To further confirm the effects of ART on $CD8^+$ T cells, we firstly conducted a qPCR assay, revealing that ART upregulated activation markers (CD69, TNFα, and IFNγ) in mouse $CD8^+$ T cells in vitro (Fig. 4A). These findings were further validated by flow cytometry (Fig. 4B), suggesting that ART augmented the effector function of $CD8^+$ T cells in vitro. The toxicity assessment of ART on $CD8^+$ T cells demonstrated selective toxicity to B16F10 cells below a concentration of 20 μM, with no significant cytotoxicity observed in $CD8^+$ T cells (Fig. 4C). Intriguingly, ferroptosis was observed in B16F10 cells but not in $CD8^+$ T cells following ART treatment, possibly attributed to distinct mRNA expression of Hmox1 in $CD8^+$ T cells and B16F10 cells (Supplementary Fig. 9).

To validate the functional impact of ART-induced $CD8^+$ T cell activation, B16F10 cells were co-cultured with $CD8^+$ T cells in the presence of ART. The cell viability of B16F10 cells was assessed using a CCK8 assay, revealing a dose-dependent promotion of $CD8^+$ T cell-mediated killing of B16F10 cells by ART (Fig. 4D). Subsequently, $CD8^+$ T cells were collected for flow cytometry analysis, demonstrating an upregulation of both $TNFα^+CD8^+$ and $IFNγ^+CD8^+$ T cells, suggesting that ART induced the activation of $CD8^+$ T cells in the co-culture system (Fig. 4E). To delve into the mechanisms underlying ART-enhanced effector function of $CD8^+$ T cells, mRNA from ART-treated mouse $CD8^+$ T cells were isolated for RNA-seq analysis, and 378 upregulated genes, 1363 downregulated genes were identified (Fig. 4F). The GO enrichment analysis revealed that DEGs were highly enriched in Regulation of T cell activation, Interferon-gamma production, Immune response, etc. (Fig. 4G). GSEA analysis revealed increased TNFα signaling via NFkB (Fig. 4H). Furthermore, our RNA-seq data supports above qPCR and flow cytometry findings, confirming that ART significantly upregulating activation markers (Cd69, Cd107a and TNFα) on mouse $CD8^+$ T cells (Supplementary Fig. 10).

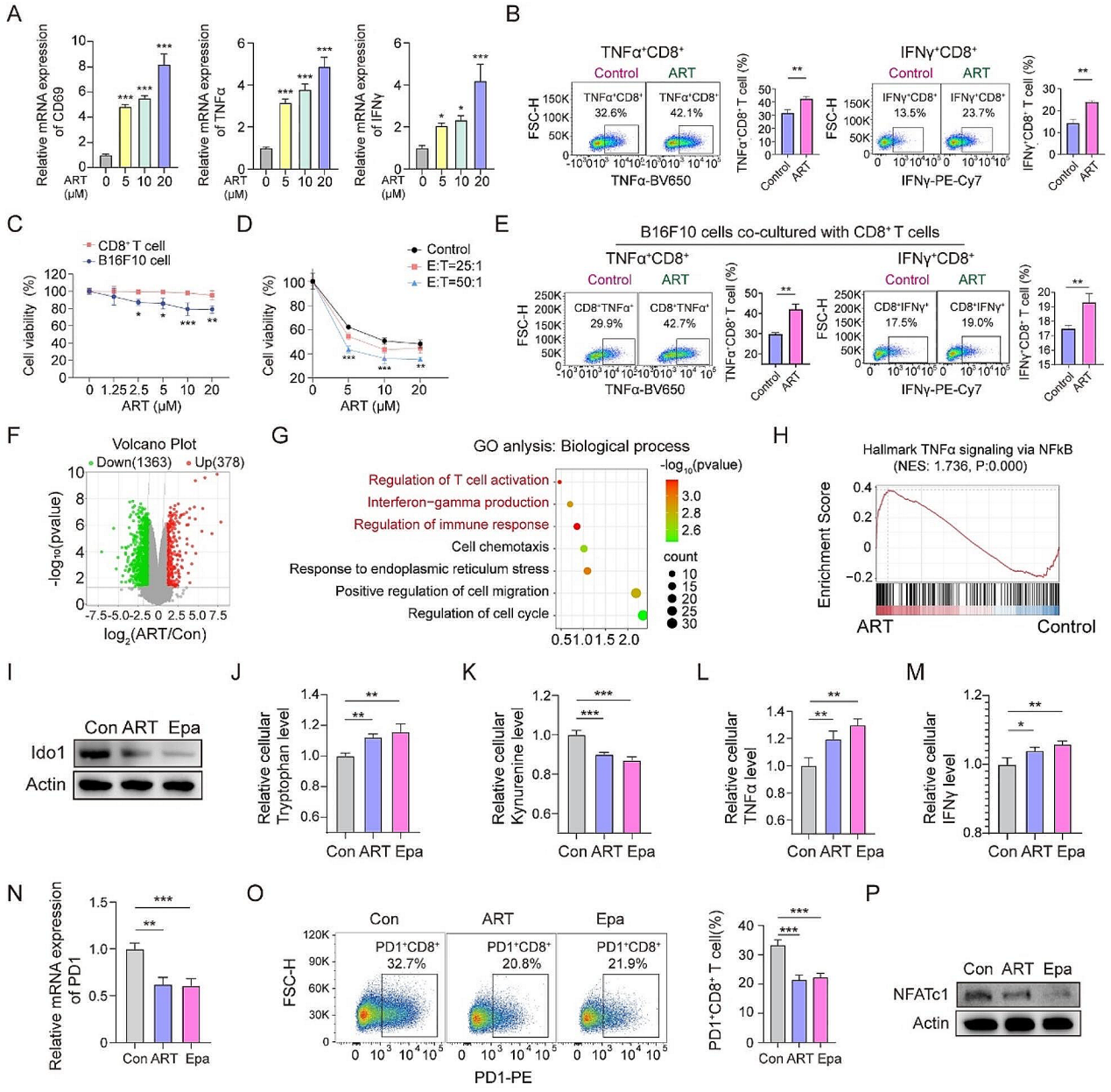

Fig. 4 ART enhanced effector function of CD8$^+$ T cells in vitro through targeting Ido1. (**A** and **B**) After mouse CD8$^+$ T cells were treated with different concentrations of ART (0, 5, 10, 20 μM), the mRNA expression of CD69, TNFα, IFNγ was detected by qPCR assay and flow cytometry. (**C**) B16F10 and CD8$^+$ T cells were treated with different concentrations of ART for 24 h, cell viability was assessed by CCK8 assay. (**D** and **E**) Co-culture assay of B16F10 cells and CD8$^+$ T cells at the ratio of 1:25/1:50 in the presence of ART for 48 h, the cell viability of B16F10 cells were measured by CCK8 assay, and the CD8$^+$ T cells were collected for flow cytometry assay to detect TNFα$^+$ CD8$^+$, IFNγ$^+$ CD8$^+$ cells. (**F**) The RNA-seq volcano plot of ART-treated CD8$^+$ T cells. (**G**) GO analysis: Biological process of DEGs. (**H**) GSEA analysis of RNA-seq. (**I**) Western blot detected the change of Ido1 in CD8$^+$ T cells after ART and Epa treatment. (**J-M**) ELISA was employed to assess the changes of Tryptophan, Kynurenine, TNFα and IFNγ in the supernatant of CD8$^+$ T cells. (**N**) qPCR detected the mRNA expression of PD1 on CD8$^+$ T cells. (**O**) Flow assay detected the expression of PD1 on CD8$^+$ T cells. (**P**) Western blot detected the change of NFATc1 in CD8$^+$ T cells. *$P < 0.05$; **$P < 0.01$; ***$P < 0.001$

We aforementioned Ido1 is the target of ART, moreover, Ido1 is reported to suppress CD8$^+$ T effector cells and facilitate an immunosuppressive microenvironment [21]. To explore if Ido1 plays a significant role in CD8$^+$ T cells, we first detected the expression of Ido1 by western blot and confirmed that both ART and Epa treatments led to decreased levels of Ido1 in CD8$^+$ T cells (Fig. 4I). ELISA analysis demonstrated that ART or Epa treatment increased Tryptophan and decreased kynurenine production in CD8$^+$ T cell supernatants (Fig. 4J-K).

Moreover, they facilitated $CD8^+$ T cells to release TNFα and IFNγ (Fig. 4L-M). Recent studies have proposed that Tryptophan enhances $CD8^+$ T cells by downregulating surface PD1 through inhibiting the transcription factor NFATc1 [32]. To ascertain whether this mechanism is universal in ART-treated $CD8^+$ T cells, we assessed PD1 and NFATc1 expression following ART or Epa treatment. The results indicated that both ART and Epa treatment significantly decreased the mRNA and expression level of PD1 (Fig. 4N-O) and also caused a marked decrease in the transcription factor NFATc1 (Fig. 4P).

ART inhibited the growth of melanoma and induced tumor cell ferroptosis in vivo

To evaluate the in vivo anti-melanoma effect of ART, B16F10 tumor-bearing mice were treated with ART (100 mg/kg/day, 200 mg/kg/day, *i.p.*). Notably, ART treatment significantly inhibited B16F10 tumor growth compared to the control group (Fig. 5A-E). Importantly, there was no notable difference in body weight between the control group and the ART-treated group (Fig. 5F), and no morphological disparities were observed in liver and kidney H&E staining between the two groups (Fig. 5G). In contrast, histopathological examination illustrated morphological changes such as nuclei shrinkage and focal necrosis in ART-treated tumor sections, otherwise, immunohistochemistry analysis demonstrated that ART decreased the expression of Ki67 (Fig. 5H), suggesting that ART inhibited the growth of melanoma.

To explore whether ART caused tumor cell ferroptosis in our mouse model, tumor sections were stained by BODIPY and we found that ART induced dose-dependently increasing of lipid peroxidation in vivo (Fig. 5I). Moreover, ART elevated Hmox1 expression while reducing the levels of Hic1 and Ido1, consistent with our in vitro findings (Fig. 5J). Together, ART inhibited the growth of melanoma and induced tumor cell ferroptosis in vivo.

ART augmented $CD8^+$ T cell-mediated antitumor immunity in vivo

To investigated whether ART enhanced effector function of $CD8^+$ T cells in vitro were applicable in vivo, single cell suspension from tumor tissues were prepared for flow cytometry analysis. Our findings revealed that ART treatment did not increase the proportion of tumor-infiltrating $CD4^+$ T cells and $CD8^+$ T cells (Supplementary Fig. 11). However, it significantly activated $CD8^+$ T cells in tumor TME, as evidenced by increased proportion of $TNFα^+$, $IFNγ^+$, $CD107a^+$ and $CD69^+$ $CD8^+$ T cells (Fig. 6A-D), accompanied by a reduction in the proportion of exhaustion-associated $PD1^+$ $CD8^+$ T cells (Fig. 6E). Immunofluorescence results further demonstrated that ART elevated TNFα and IFNγ levels while decreasing PD1 level in tumors (Fig. 6F). However, these activation and exhaustion markers were unaffected in $CD4^+$ T cells (Supplementary Fig. 12). Collectively, ART enhanced the antitumor immunity of $CD8^+$ T cells, which synergized with ART-induced tumor cell ferroptosis *in vivo*.

To further explore the essential role of $CD8^+$ T cells in the anti-tumor effects of ART in vivo, B16F10 tumor-bearing mice were *i.p.* received the neutralizing anti-CD8 antibody to deplete the $CD8^+$ T cells (Fig. 6G). The potent efficacy of $CD8^+$ T cell depletion in mouse blood was confirmed by flow cytometry (Fig. 6H) and immunohistochemical staining of mouse tumor (Fig. 6I). Our results revealed that $CD8^+$ T cell depletion slightly accelerated tumor growth in mice without ART treatment, but significantly reversed the tumor growth inhibited by ART (Fig. 6J-K). These results strongly suggest that $CD8^+$ T cells play a pivotal role in the antitumor effects of ART in the B16F10 melanoma model.

Discussion

Ferroptosis, a non-apoptotic, iron-dependent form of cell death, is characterized by three major characteristics: iron accumulation, lipid peroxidation, and the accumulation of malondialdehyde (MDA), a representative end-product of lipid peroxidation. Uncontrolled proliferation is a fundamental driver of malignancy development, and inhibiting cell proliferation is an effective strategy for tumor control. Emerging evidence suggests that ferroptosis functions as a novel cancer suppressor in cancer cell proliferation [33] and development [34]. Ferroptosis is intriguing because many cancer cells are susceptible to it, and can be widely seen in chemotherapy, radiotherapy, and immunotherapy, highlighting its potential as a viable strategy for cancer treatment [35, 36]. Recently, various natural compounds, including Artemisinin, a sesquiterpene lactone compound with a unique peroxide bridge, have been reported to sensitize tumor cells to ferroptosis. Artesunate (ART), a water-soluble semi-synthetic derivative of artemisinin, which has been reported to react with iron, triggering reactive oxygen species (ROS) production and resulting in tumor cell ferroptosis, without inducing apoptosis or necroptosis. Additionally, ART has demonstrated synergy with sorafenib in inducing ferroptosis in hepatocellular carcinoma [37]. Although ART has been previously identified as a potential ferroptosis inducer, the precise mechanism remains unclear. In our study, we confirmed that ART triggered ferroptosis by enhancing intracellular ROS accumulation, lipid peroxidation and MDA production in melanoma B16F10 cells and SK-MEL-28 cells. Moreover, we found that ART inhibited the proliferation of these melanoma cells by inducing cell cycle arrest at the G2/M phase. These findings suggest that ART is a promising anti-melanoma compound

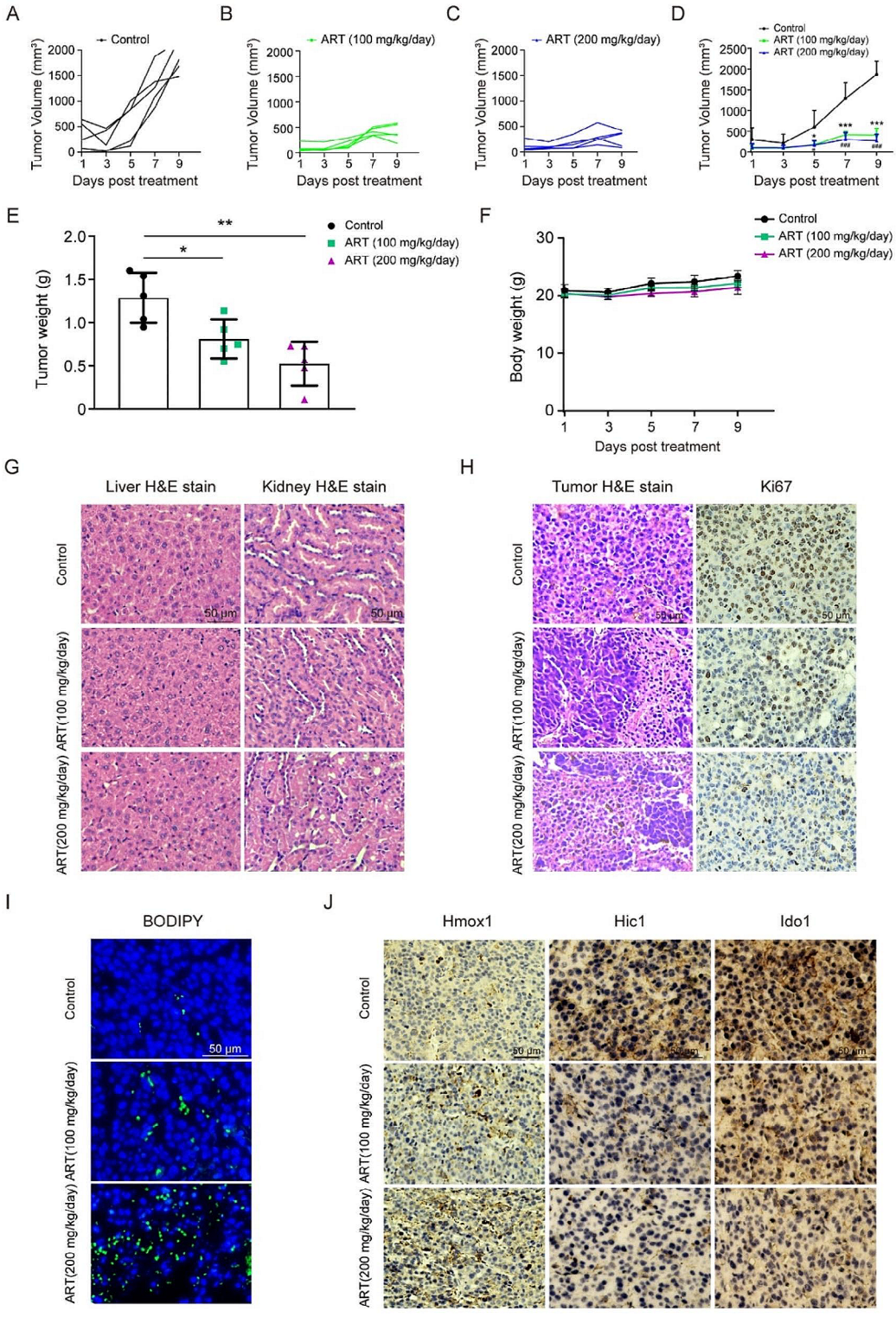

Fig. 5 ART inhibited the growth of melanoma and induced tumor cell ferroptosis *in vivo*. B16F10 cells were inoculated into C57 mice subcutaneously, mice were divided into 3 groups (Control, ART (100 mg/kg/day), ART (200 mg/kg/day)) (**A-D**) Tumor growth curve of each group. (**E**) Tumor weight of each group. (**F**) Body weight of each group. (**G**) Liver and Kidney H&E staining. (**H**) H&E stain of tumors, immunohistochemistry of Ki67. (**I**) Immunofluorescence of BODIPY stained tumor sections. (**J**) Immunohistochemistry of Hmox1, Hic1 and Ido1 expression in tumor sections. $^{*}P<0.05$; $^{**}P<0.01$; $^{***}P<0.001$; $^{\#}P<0.05$; $^{\#\#\#}P<0.001$

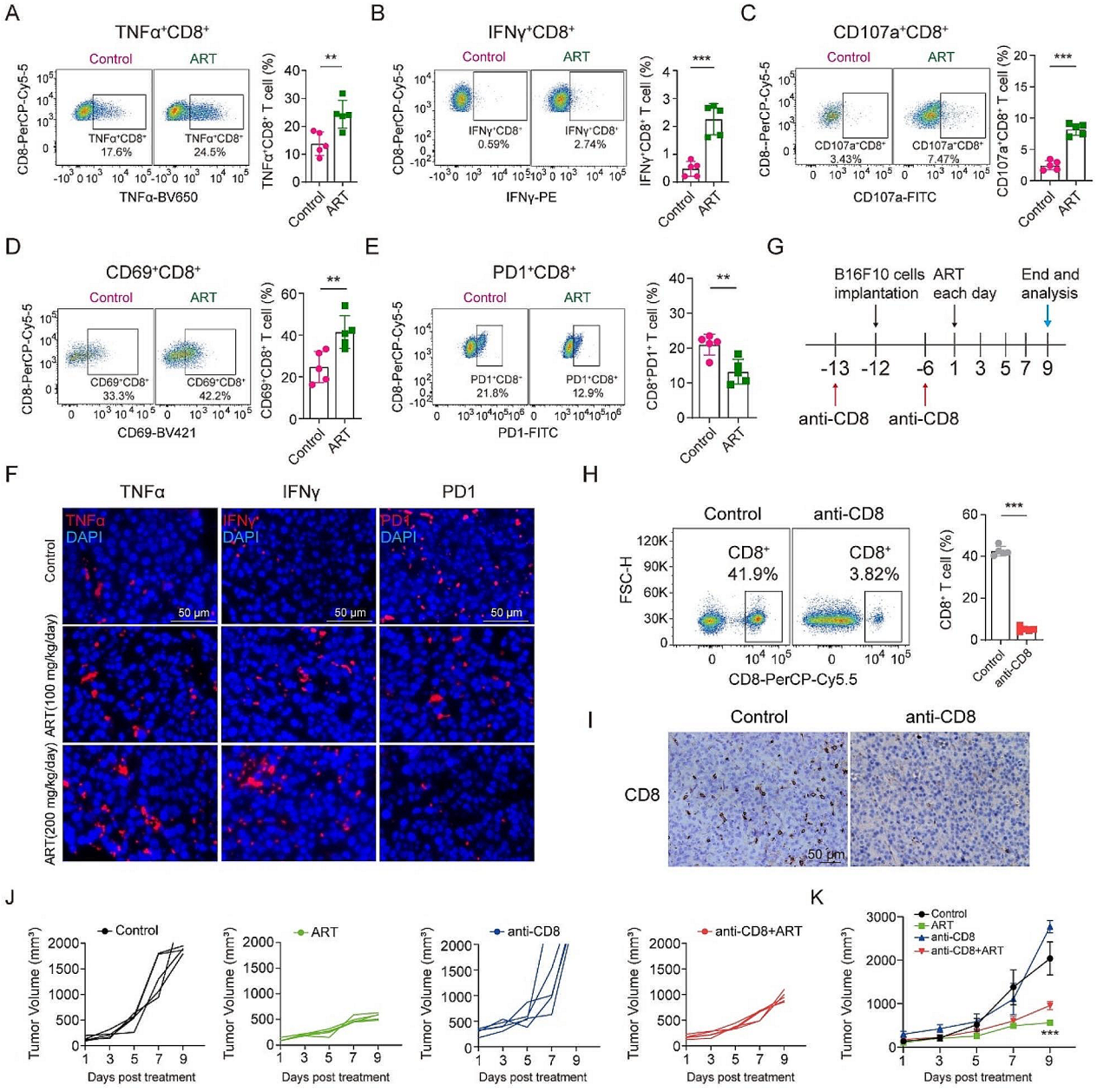

Fig. 6 ART augmented CD8$^+$ T cell-mediated antitumor immunity *in vivo*. (**A-E**) Flow cytometric analysis of the proportion of TNFα$^+$, IFNγ$^+$, CD107a$^+$, CD69$^+$ or PD1$^+$ CD8$^+$ T cells in B16F10 tumors. (**F**) Immunofluorescence of TNFα, IFNγ and PD1 in tumor sections. (**G**) The schematic diagram of CD8 depletion strategy in B16F10-bearing mice. Anti-CD8 antibody treatment was initiated on day − 13 and − 6 prior to ART administration (100 mg/kg/day for 9 days). (**H**) Flow cytometry was used to confirm the depletion efficacy of CD8$^+$ T cells in mouse blood. (**I**) Immunohistochemical staining of mouse tumor to evaluate the depletion efficacy of CD8$^+$ T cells. (**J**) Tumor growth curve of each mouse in different group. (**K**) Average of tumor volume of each group. $^{**}P < 0.01$; $^{***}P < 0.001$

capable of simultaneously inducing ferroptosis and inhibiting cell proliferation.

Hmox1 is an endoplasmic reticulum (ER)-anchored enzyme which metabolizes heme into pro-oxidant ferrous iron, carbon monoxide and anti-oxidant biliverdin. Increasing evidence indicates that upregulation of Hmox1 induces iron overload, leading to lipid peroxidation and ferroptosis. Studies have reported that ART induces oxidative stress, resulting in the upregulation of Hmox1 and triggering ART's toxicity [38]. In our study, through RNA-seq analysis and genetic manipulation, we identified Hmox1 as a key target in ART-induced melanoma cell ferroptosis. Hmox1 overexpression significantly enhanced, while Hmox1 knockout significantly

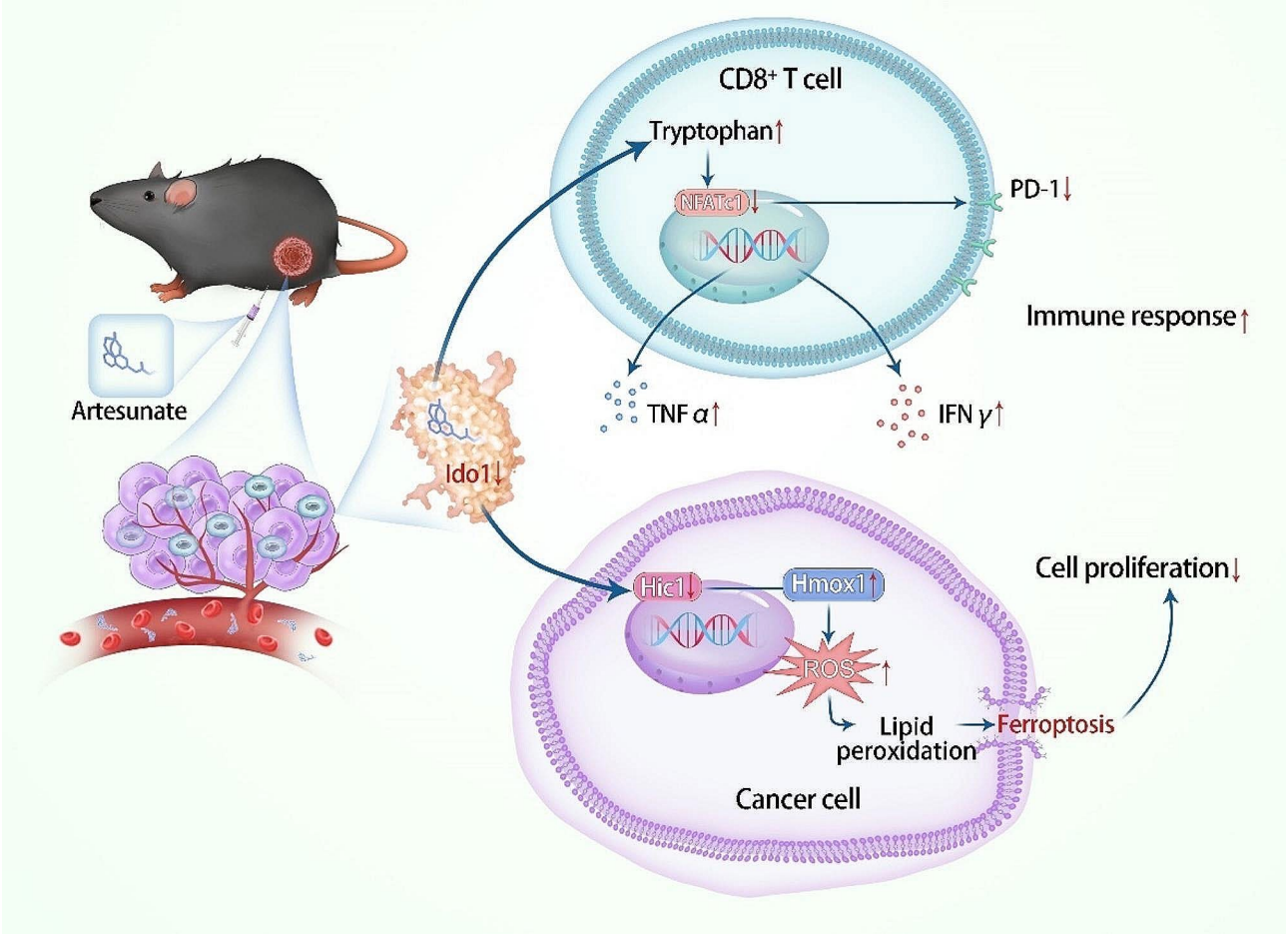

Fig. 7 Schematic illustrating the synergistic effect of ART in inducing tumor cell ferroptosis and activating $CD8^+$ T cell-mediated anti-tumor immunity. (1) In B16F10 cells, ART directly targets Ido1, decreasing the level of Hic1, promoting the transcription of Hmox1, facilitating the ROS production and lipid peroxidation, inducing ferroptosis of melanoma cells, resulting in cell proliferation inhibition of melanoma; (2) In $CD8^+$ T cells, ART directly targets Ido1, leading to the accumulation of tryptophan and a decrease in NFATc1 level, thereby inhibiting the transcription of PD1, activating $CD8^+$ T cells to secrete TNFα and IFNγ, ultimately enhancing its anti-tumor efficacy

suppressed ART-induced ferroptosis. Moreover, we revealed for the first time that ART-enhanced Hmox1 transcription is dependent on the downregulation of the transcriptional suppressor Hic1. Additionally, we identified ART as a novel Ido1 inhibitor through molecular docking, CETSA and SPR assays. Ido1 has been reported to propagate anti-ferroptotic signaling, including enhancing ROS scavenging, activating NRF2 and aryl hydrocarbon receptor cell-protective pathway [39]. Consistent with this study, we further uncovered that ART targets Ido1, inhibiting Hic1, promoting Hmox1-mediated lipid peroxidation and melanoma cell ferroptosis [40–42]. The potent anti-melanoma efficacy of ART and the mechanistic insights into ART-induced melanoma cell ferroptosis through the Ido1/Hic1/Hmox1 pathway were also validated in a B16F10 tumor-bearing mouse model.

Ido1 has also been reported to be highly expressed in multiple types of human cancer, demonstrating a negative correlation with patient prognosis. It functions as an immunosuppressive regulator in the TME, which can convert tryptophan into kynurenine, thereby inhibiting $CD8^+$ T cells, NK cells and activating regulatory T cells, facilitating tumor cell evasion. We aforementioned ART as an Ido1 inhibitor guided us to explore whether ART activates anti-tumor immunity, and we found that ART could also targets Ido1 in $CD8^+$ T cells, inhibiting the transition of tryptophan to kynurenine, decreasing the immune inhibitory receptor PD1 expression, and activating $CD8^+$ T cell to release cytokines in vitro. Combined with the RNA-seq data, GSEA analysis and our in vitro results, we thought that TNFα releasing may play a significant role in ART-induced $CD8^+$ T cell activation. Furthermore, in B16F10 tumor-bearing mouse model, although ART did not significantly increase T cell infiltration into tumors, it effectively activated $CD8^+$ T cell-mediated antitumor immunity. Notably, $CD8^+$ T cell depletion in the mouse model demonstrated that ART-activated $CD8^+$ T cell-mediated anti-tumor immunity,

coupled with its induction of tumor cell ferroptosis, generated a synergistic anti-tumor effect in vivo. Interestingly, our study revealed that ART selectively induces ferroptosis in melanoma cells but not in $CD8^+$ T cells, probably attributed to the much higher expression of its ferroptosis-inducing target, Hmox1, in melanoma cells compared to $CD8^+$ T cells. This selective induction of ferroptosis property affords ART as a promising candidate for development and application in cancer treatment.

Conclusions

In summary, our investigation reveals that ART demonstrates potent in vitro and in vivo anti-melanoma efficacy by inhibiting tumor cell proliferation, inducing ferroptosis, and activating anti-tumor immunity. Mechanistically, in tumor cells, ART directly targets Ido1, thereby suppressing Hic1-mediated transcription suppression of Hmox1, resulting in ferroptosis. In $CD8^+$ T cells, ART also targets Ido1 to increase tryptophan, leading to the inhibition of NFATc1-mediated PD1 transcription and ultimately activating $CD8^+$ T cells (Fig. 7). This study provides a novel mechanistic basis for the utilization of ART as an Ido1 inhibitor and application in clinical melanoma treatment.

Abbreviations

ART	Artesunate
TCM	Traditional Chinese medicine
TME	Tumor microenvironment
Ido1	Indoleamine2,3-dioxygenase 1
Trp	Tryptophan
Kyn	Kynurenine
Tregs	Regulatory T cells
Fer-1	Ferrostatin-1
CCK-8	Cell counting kit-8
DEGs	Differentially expressed genes
GSEA	Gene set enrichment analysis
NES	Normalized enrichment score
FDR	False discovery rate
MFI	Mean fluorescence intensity
MDA	Malondialdehyde
CHIP	Chromatin immunoprecipitation
SPR	Surface plasmon resonance
CETSA	Cellular thermal shift assay
Epa	Epacadostat
ROS	Reactive oxygen species
ER	Endoplasmic reticulum

Supplementary Information

The online version contains supplementary material available at https://doi.org/10.1186/s12964-024-01759-8.

Supplementary Material 1

Acknowledgements

Not applicable.

Author contributions

G.L. and R.Z. conceptualized and designed the study. W.L., H.Z., performed experiments and analyzed data. W.L., C.H., Q.W. and C.Y. conducted the flow cytometric and animal experiments. C.L., M.Y. and M.H. analyzed the data. W.L. and G.L. wrote the manuscript. All authors approved the final version of the manuscript.

Funding

This research was supported by National Natural Science Foundation of China (82104453, 82150113); Chongqing Talent Program-Leading Innovative Talents (CQYC20210303411); the Chongqing Key Specialty Construction Project of Clinical Pharmacy (Clinical Pharmacy of Medical oncology).

Data availability

No datasets were generated or analysed during the current study.

Declarations

Ethics approval and consent to participate

Animal experiments were performed adhering to the guidelines of the Animal Care and Use Committee of Army Medical University (NO. AMUWEC20210099) and conducted according to the institutional guidelines.

Consent for publication

Not applicable.

Competing interests

The authors declare no competing interests.

Received: 11 June 2024 / Accepted: 21 July 2024
Published online: 26 July 2024

References

1. Shain AH, et al. From melanocytes to melanomas. Nat Rev Cancer. 2016;16(6):345–58.
2. Egeler MD et al. Survival is not enough: understanding the mental burden of cutaneous melanoma. Br J Dermatol. 2024.
3. Hirschhorn T, et al. The development of the concept of ferroptosis. Free Radical Bio Med. 2019;133:130–43.
4. Wu XG, et al. Ferroptosis as a novel therapeutic target for cardiovascular disease. Theranostics. 2021;11(7):3052–9.
5. Zhou W, et al. Verteporfin induces lipid peroxidation and ferroptosis in pancreatic cancer cells. Free Radic Biol Med. 2024;212:493–504.
6. Huang W, et al. Yi-qi-Hua-Yu-Jie-Du decoction induces ferroptosis in cisplatin-resistant gastric cancer via the AKT/GSK3beta/NRF2/GPX4 axis. Phytomedicine. 2024;123:155220.
7. Newman DJ, et al. Natural products as sources of new drugs over the period 1981–2002. J Nat Prod. 2003;66(7):1022–37.
8. Jiang W, et al. Artesunate attenuated progression of atherosclerosis lesion formation alone or combined with rosuvastatin through inhibition of pro-inflammatory cytokines and pro-inflammatory chemokines. Phytomedicine. 2016;23(11):1259–66.
9. Efferth T, et al. The anti-malarial artesunate is also active against cancer. Int J Oncol. 2001;18(4):767–73.
10. Efferth T, et al. Detection of apoptosis in KG-1a leukemic cells treated with investigational drugs. Arzneimittelforschung. 1996;46(2):196–200.
11. Lai H, et al. Selective cancer cell cytotoxicity from exposure to dihydroartemisinin and holotransferrin. Cancer Lett. 1995;91(1):41–6.
12. von Hagens C, et al. Long-term add-on therapy (compassionate use) with oral artesunate in patients with metastatic breast cancer after participating in a phase I study (ARTIC M33/2). Phytomedicine. 2019;54:140–8.
13. Trimble CL, et al. A first-in-human proof-of-concept trial of intravaginal artesunate to treat cervical intraepithelial neoplasia 2/3 (CIN2/3). Gynecol Oncol. 2020;157(1):188–94.
14. Deeken JF, et al. A phase I study of intravenous artesunate in patients with advanced solid tumor malignancies. Cancer Chemother Pharmacol. 2018;81(3):587–96.
15. Chen J, et al. Single-cell transcriptome analysis reveals the regulatory effects of artesunate on splenic immune cells in polymicrobial sepsis. J Pharm Anal. 2023;13(7):817–29.
16. Cao D, et al. Artesunate promoted anti-tumor immunity and overcame EGFR-TKI resistance in non-small-cell lung cancer by enhancing oncogenic TAZ degradation. Biomed Pharmacother. 2022;155:113705.

17. Liu M, et al. Targeting the IDO1 pathway in cancer: from bench to bedside. J Hematol Oncol. 2018;11(1):100.
18. Theate I, et al. Extensive profiling of the expression of the indoleamine 2,3-dioxygenase 1 protein in normal and tumoral human tissues. Cancer Immunol Res. 2015;3(2):161–72.
19. Godin-Ethier J, et al. Indoleamine 2,3-dioxygenase expression in human cancers: clinical and immunologic perspectives. Clin Cancer Res. 2011;17(22):6985–91.
20. Munn DH, et al. Potential regulatory function of human dendritic cells expressing indoleamine 2,3-dioxygenase. Science. 2002;297(5588):1867–70.
21. Mezrich JD, et al. An interaction between kynurenine and the aryl hydrocarbon receptor can generate regulatory T cells. J Immunol. 2010;185(6):3190–8.
22. Munn DH, et al. GCN2 kinase in T cells mediates proliferative arrest and anergy induction in response to indoleamine 2,3-dioxygenase. Immunity. 2005;22(5):633–42.
23. Fallarino F, et al. The combined effects of tryptophan starvation and tryptophan catabolites down-regulate T cell receptor zeta-chain and induce a regulatory phenotype in naive T cells. J Immunol. 2006;176(11):6752–61.
24. Platten M, et al. Tryptophan metabolism as a common therapeutic target in cancer, neurodegeneration and beyond. Nat Rev Drug Discov. 2019;18(5):379–401.
25. Chen S, et al. The ups, downs and new trends of IDO1 inhibitors. Bioorg Chem. 2021;110:104815.
26. Kelly CM, et al. A phase II study of Epacadostat and Pembrolizumab in patients with Advanced Sarcoma. Clin Cancer Res. 2023;29(11):2043–51.
27. Subramanian A, et al. Gene set enrichment analysis: a knowledge-based approach for interpreting genome-wide expression profiles. Proc Natl Acad Sci U S A. 2005;102(43):15545–50.
28. Olivo Pimentel V, et al. A novel co-culture assay to assess anti-tumor CD8(+) T cell cytotoxicity via luminescence and multicolor flow cytometry. J Immunol Methods. 2020;487:112899.
29. Chin CH, et al. cytoHubba: identifying hub objects and sub-networks from complex interactome. BMC Syst Biol. 2014;8(Suppl 4):S11.
30. Nickel J, et al. SuperPred: update on drug classification and target prediction. Nucleic Acids Res. 2014;42(Web Server issue):W26–31.
31. Su LJ, et al. Reactive Oxygen species-Induced lipid peroxidation in apoptosis, Autophagy, and Ferroptosis. Oxid Med Cell Longev. 2019;2019:5080843.
32. Qin R et al. Tryptophan potentiates CD8(+) T cells against cancer cells by TRIP12 tryptophanylation and surface PD-1 downregulation. J Immunother Cancer. 2021;9(7).
33. Yang X, et al. Fish oil-based microemulsion can efficiently deliver oral peptide blocking PD-1/PD-L1 and simultaneously induce ferroptosis for cancer immunotherapy. J Control Release. 2024;365:654–67.
34. Sun S, et al. Targeting ferroptosis opens new avenues for the development of novel therapeutics. Signal Transduct Target Ther. 2023;8(1):372.
35. Xu T, et al. Molecular mechanisms of ferroptosis and its role in cancer therapy. J Cell Mol Med. 2019;23(8):4900–12.
36. Mou Y, et al. Ferroptosis, a new form of cell death: opportunities and challenges in cancer. J Hematol Oncol. 2019;12(1):34.
37. Li ZJ, et al. Artesunate synergizes with sorafenib to induce ferroptosis in hepatocellular carcinoma. Acta Pharmacol Sin. 2021;42(2):301–10.
38. Jochims F et al. The Antimalarial Drug Artesunate mediates selective cytotoxicity by upregulating HO-1 in Melanoma cells. Biomedicines. 2023;11(9).
39. Fiore A, et al. Kynurenine importation by SLC7A11 propagates anti-ferroptotic signaling. Mol Cell. 2022;82(5):920–32. e7.
40. Xu J, et al. The dual role and mutual dependence of heme/HO-1/Bach1 axis in the carcinogenic and anti-carcinogenic intersection. J Cancer Res Clin Oncol. 2023;149(1):483–501.
41. Chiang SK et al. A dual role of Heme Oxygenase-1 in Cancer cells. Int J Mol Sci. 2018;20(1).
42. Gamage SMK, et al. Dual role of heme iron in cancer; promotor of carcinogenesis and an inducer of tumour suppression. Exp Mol Pathol. 2021;120:104642.

Publisher's Note